JGR Earth Surface

RESEARCH ARTICLE
10.1029/2021JF006349

Radar Derived Subglacial Properties and Landforms Beneath Rutford Ice Stream, West Antarctica

Rebecca Schlegel[1], Tavi Murray[1], Andrew M. Smith[2], Alex M. Brisbourne[2], Adam D. Booth[3], Edward C. King[2], and Roger A. Clark[3]

[1]Glaciology Group, Department of Geography, Swansea University, Swansea, UK, [2]British Antarctic Survey, Natural Environment Research Council, Cambridge, UK, [3]Institute of Applied Geoscience, School of Earth and Environment, University of Leeds, Leeds, UK

Key Points:

- Glacier bed properties (water content, porosity) are constrained using surface radar data calibrated with seismic acoustic impedance
- Results show sequences of low porosity material (consolidated sediment or rock), soft sediment and free-water beneath Rutford Ice Stream
- Mega-scale glacial lineations are pervasive beneath ice streams, some with a free water layer >10 km long and 100 m wide along their crest

Supporting Information:

Supporting Information may be found in the online version of this article.

Correspondence to:

R. Schlegel,
967901@swansea.ac.uk

Citation:

Schlegel, R., Murray, T., Smith, A. M., Brisbourne, A. M., Booth, A. D., King, E. C., & Clark, R. A. (2022). Radar derived subglacial properties and landforms beneath Rutford Ice Stream, West Antarctica. *Journal of Geophysical Research: Earth Surface*, *127*, e2021JF006349. https://doi.org/10.1029/2021JF006349

Received 10 JUL 2021
Accepted 20 DEC 2021

Abstract Basal properties beneath ice streams and glaciers are known to be a control for ice flow dynamics, hence knowledge of them is crucial for predicting sea level due to changes in glacial dynamics. Basal properties, processes and topography also drive the formation of subglacial landforms. Bed properties beneath Rutford Ice Stream (West Antarctica) have previously been described using seismic acoustic impedance measurements at a sparse spatial coverage. Here, we derive bed properties in a 15 × 17 km grid of surface radar data with coverage and sampling much higher than previous seismic studies. Bed reflection amplitudes in surface radar data were calibrated using sediment porosities (ranging from 0.4–0.5) derived from seismic acoustic impedance. We find the bed properties are spatially variable, consisting of low porosity material in some areas and soft sediment in other areas. Comparison of seismic and surface radar data imply the low porosity material to be a consolidated sediment or sedimentary rock. Mega-scale glacial lineations (MSGLs) are ubiquitous on the bed and consist of soft, high porosity, probably deforming sediment, consistent with previous interpretations of MSGLs. We find some MSGLs have high reflectivity on their crest, interpreted as water bodies overlying high porosity sediment, whereas the trough around and the upstream end of some landforms consist of low porosity material. Integrating these different observations, we place constraints on possible explanations for the occurrence of water on the crest of landforms.

Plain Language Summary Physical properties of rocks and sediments as well as the presence of water beneath ice streams and glaciers control the flow of the ice. Understanding glacial flow is important to better constrain predictions of sea-level changes. Within this study we present physical properties of material beneath Rutford Ice Stream in West Antarctica over a 15 × 17 km area. Our data show areas of high porosity interpreted as wet sediment and areas of low porosity beneath the ~2 km thick ice stream. Ice movement above areas of soft sediment is assumed to be maintained by sediment deformation, whereas in areas overlain by low porosity material, sliding of the ice over this material is assumed to maintain flow. The topography beneath Rutford Ice Stream shows many elongated landforms, some over 14 km long. We show that these landforms partly consist of soft sediment. Some of these seem to have a water layer on their crest, but it is not well understood why. However, there might be variations in the sediment composition of the landforms enabling the creation of this water layer. The occurrence of materials with different properties and water show us how heterogenous the bed beneath ice streams can be, which is important for modeling ice stream motion.

1. Introduction

Over 90% of the mass of the West Antarctic Ice Sheet is transported by fast flowing ice streams that drain ice from the interior of the ice sheet to the oceans (Bamber et al., 2000; Rignot, 2008). Such fast flow is facilitated by the active deformation of water-saturated sediment and by sliding over consolidated beds or crystalline bedrock (Cuffey & Paterson, 2010). Subglacial water has a major impact on the dynamics of West Antarctic ice streams by facilitating till deformation as well as reducing basal friction and therefore enhancing sliding (Blankenship et al., 2001; Siegert et al., 2018). Typical models of subglacial water systems include water storage at the lee side of bedrock features (Kamb, 2001), in subglacial channels, water films or canals (Cuffey & Paterson, 2010).

Subglacial landforms such as mega-scale glacial lineations (MSGLs) and drumlins are generated by processes at the ice-bed interface and are a key component of the subglacial environment. Several models describe the theoretical formation of these landforms, but consensus has yet to be achieved. Possible models explaining

their formation include keels of ice plowing furrows (Clark et al., 2003), meltwater floods (Shaw et al., 2008) and instability theories (Schoof & Clarke, 2008). Although many landforms have been observed in deglaciated terrains and in the marine record (e.g., Dowdeswell et al., 2016; Ely et al., 2016; Spagnolo et al., 2014), relatively few studies so far reveal in situ observations of landforms beneath actively flowing ice, but the number of observations is increasing (Clyne et al., 2020; King et al., 2007; Riverman et al., 2019; Smith, 1997a; Smith & Murray, 2009). Moreover, knowledge of in situ subglacial conditions and the ice flow in such environments is crucial to understand the processes involved in landform formation.

Present basal conditions, and their spatial pattern, can be studied using radar waves. Radar reflection characteristics are influenced by the presence and thickness of basal water layers as well as basal roughness (Copland & Sharp, 2001). Previous studies from various locations have analyzed the bed-reflection power (BRP) to determine the distribution of cold- and warm-based glacier ice (Copland & Sharp, 2001), to identify subglacial lakes, canals or channels (Murray et al., 2008; Siegert & Ridley, 1998), and to distinguish between frozen and wet beds in Antarctica (Bentley et al., 1998; Gades et al., 2000).

The combination of airborne as well as surface radar together with active seismic data enables a detailed study of basal processes, and different resolution of these data types broadens the potential for understanding subglacial conditions. Nevertheless, comparisons between seismic and radar data are not straightforward given the different controls on electromagnetic and seismic wave propagation. Radar wave propagation is controlled by electromagnetic properties, like the relative dielectric permittivity, while seismic wave propagation is influenced by the mechanical properties of the material. Various properties, such as density, conductivity, cohesion, crystal orientation and temperature (liquid water content) impact both the electromagnetic and mechanical properties. Water is a key influence since its affect on wave velocity and attenuation rates differ strongly between seismic and radar waves. Due to the sensitivity of radar waves to the occurrence of water, radar surveys are often used to investigate water distribution at the bed as well as water inclusion in ice (Navarro et al., 2005). Despite the challenges of merging seismic and radar data, previous studies (e.g., Endres et al., 2009; Ghose & Slob, 2006) demonstrate the potential of combining seismic and radar data to obtain information about properties in the subsurface.

In this study we present surface radar data with a dense spatial coverage to infer bed properties. Radar reflectivity is calibrated using properties inferred from overlapping seismic and airborne radar data. Seismic acoustic impedance (the product of seismic velocity and density) allowed inference of sediment properties, including porosity, which was used to calibrate surface radar reflectivity and calculate sediment porosity throughout the surface radar data set.

2. Rutford Ice Stream and Data

Rutford Ice Stream (RIS) in West Antarctica (Figure 1a) has been studied extensively over the last four decades (Doake et al., 1987; King et al., 2016; Murray et al., 2008; Smith, 1997a). RIS drains into the Ronne Ice Shelf, having ice flow speed of around 380 m a^{-1} at our study site (Murray et al., 2007) and bounded by the Ellsworth Mountains and the Fletcher Promontory to the west and east, respectively (Figure 1a). RIS occupies a 2.2 km deep and 26 km wide asymmetric valley (Figure 1b), and has sediment at the bed that is interpreted to be water-saturated and at the pressure-melting point (Smith & Murray, 2009). Seismic acoustic impedance measurements indicate a transition from soft sediment upstream to stiff, non-deforming sediment downstream (Smith, 1997a; Smith & Murray, 2009; Smith et al., 2007). The red dashed line in Figure 1b shows an interpretation of the spatial boundary separating soft and stiff sediment (King et al., 2009), defined by comparing the distribution of surface radar reflectivity acquired in 2007/08 to that of soft and stiff sediment inferred from seismic acoustic impedance. Along with a change in sediment properties the flow mechanism has been interpreted to change from basal motion accommodated by sediment deformation (high sediment porosity ~0.4 to 0.45) to basal sliding (lower sediment porosity ~0.3) across this boundary (Smith, 1997a; Smith & Murray, 2009; Smith et al., 2007). A change in bed properties and flow mechanism is supported by the character of microseismic events in the region (Kufner et al., 2021; Smith et al., 2015).

Observations over the past ~25 years show no evidence for any long-term changes in ice flow speed (Gudmundsson, 2006; Gudmundsson & Jenkins, 2009; Murray et al., 2007; Vaughan et al., 2008), which implies temporal consistency in basal conditions (like water film thickness). Repeated acoustic impedance measurements indicate

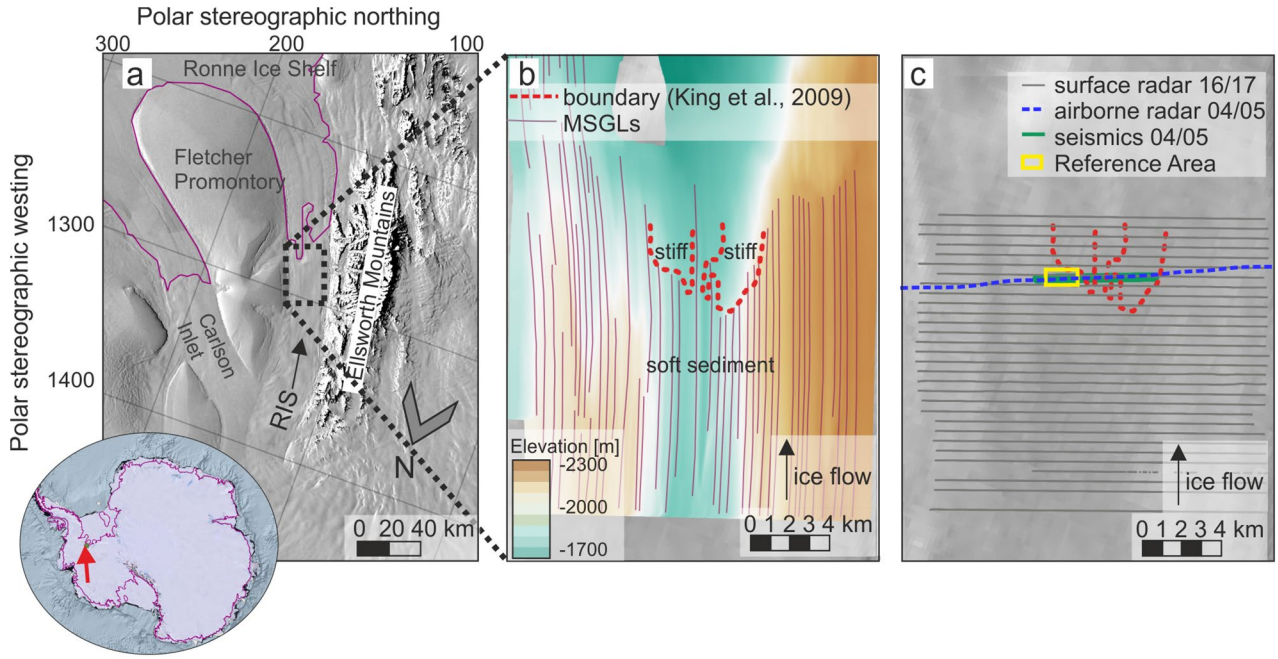

Figure 1. Overview of Rutford Ice Stream (RIS). (a) Satellite image of RIS (Landsat Image Mosaic of Antarctica) and the surrounding Ellsworth Mountains and Fletcher Promontory. ASAID Grounding line (Bindschadler et al., 2011) is shown in purple. Dashed black box marks the area shown in (b) and (c). (b) Basal topography of RIS, purple lines highlight interpreted MSGLs (King et al., 2016). Red line is the interpretation of the boundary between soft and stiff sediment by King et al. (2009). (c) Location of the surface radar lines (gray), seismic line (green) and airborne radar line (blue dashed). Yellow box marks the Reference Area for the calibration of surface radar data.

only very localized temporal changes in bed properties and imply temporal consistency across the majority of areas sampled (Smith & Murray, 2009; Smith et al., 2007).

The bed of RIS has numerous MSGLs (Figure 1b and King et al., 2009), including one termed the "Bump", a 550 m wide and 53 m high feature in the center of the ice stream. Smith et al. (2007) identified a subglacial landform of dimensions 10 m height and 100 m width that developed over a period of seven years and subsequent studies showed this landform to be a MSGL (King et al., 2016). We refer to this feature as MSGL 3 (Figure 2a).

2.1. Data Acquisition of Surface Radar Data in 2016/17

Surface radar data were acquired in 2016/17 as part of the BEAMISH project (Smith et al., 2020), using the British Antarctic Survey (BAS) DELORES system (King et al., 2007) towed behind a snowmobile. This system has a half-dipole length of 20 m and radiates energy with a center-frequency of ~3 MHz. An area of 15 × 17 km of the 26 km wide ice stream was surveyed, including 31 parallel 17 km long lines, spaced at ~500 m and acquired orthogonal to ice flow (gray lines Figure 1c). A sledge at the midpoint between receiver and transmitter was equipped with a dual-frequency GPS receiver to provide accurate positions for post-processing.

2.2. Current Understanding of Bed Properties Under RIS

Calibration and validation of the 2016/17 surface radar reflectivity is based on airborne radar (blue dashed line Figure 1c) and seismic acoustic impedance data (green line) acquired on RIS in 2004/05. These data have been described and interpreted in Murray et al. (2008) and Smith et al. (2007); Smith and Murray (2009), respectively, and a brief summary is presented here, with results and interpretation shown in Figure 2.

2.2.1. Airborne Radar Data

Several lines of airborne radar data (PASIN, 150 MHz center frequency) were acquired in 2004/05, although only line R2 of Murray et al. (2008) intersects with both seismic and surface radar profiles (Figure 1c). The amplitude of the bed reflection was calibrated using the reflection of the floating part of the Carlson Inlet (Figure 1a), where

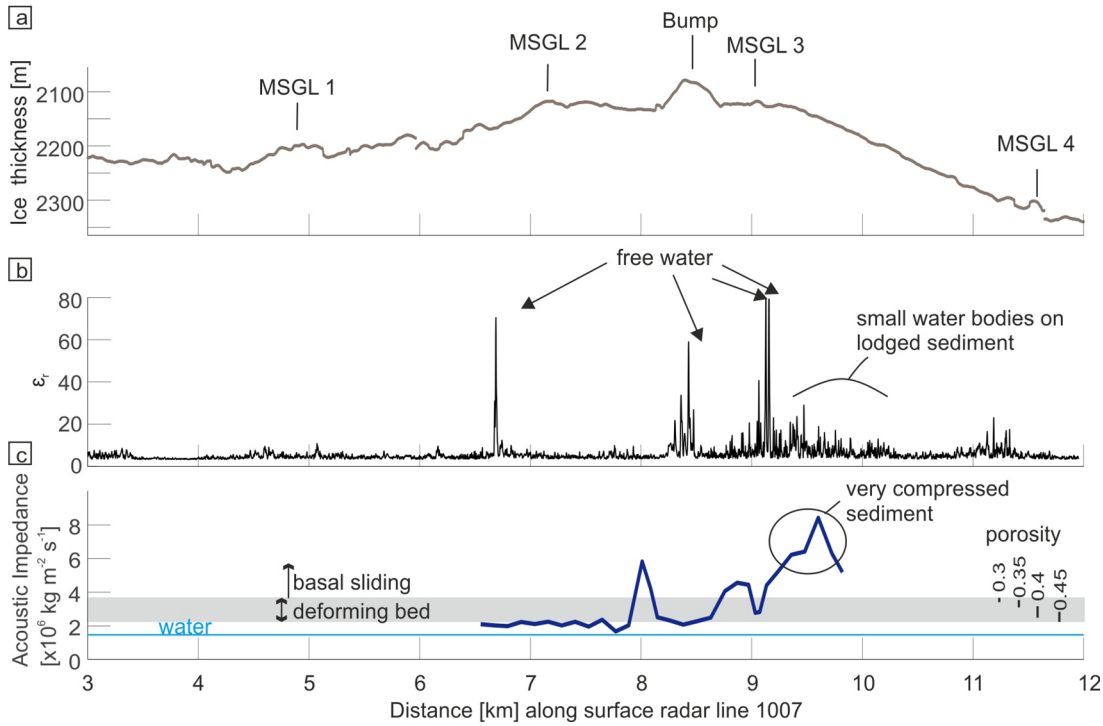

Figure 2. Results and interpretation from previous studies on bulk relative dielectric permittivity and acoustic impedance of the Rutford Ice Stream bed. (a) Bed topography with landforms annotated, (b) relative dielectric permittivity from airborne radar (Murray et al., 2008) and (c) acoustic impedance with possible porosity ranges (Smith & Murray, 2009; Smith et al., 2007). The gray box shows acoustic impedance values of 2.2–3.8 × 10^6 kg m^{-2} s^{-1}, corresponding to soft, deformable sediment. The cyan line shows acoustic impedance of water (~1.5 × 10^6 kg m^{-2} s^{-1}).

electrical properties either side of the basal reflection (ice and water) can be assumed (Murray et al., 2008). 50 traces were stacked and recorded every 40 cm along track, and thereafter smoothed using a 20-trace (~8 m) running mean.

Interpretations of airborne radar data (Murray et al., 2008) include four spots of high reflectivity, interpreted as water at the ice-bed interface (bulk relative dielectric permittivity = 80), at 6.8, 8.5, 9.1 and 9.4 km (Figure 2). Two of these are located on the crests of landforms (Bump and MSGL 3). Murray et al. (2008) also explain peaks in bulk relative dielectric permittivity above 10, in areas where the bed is assumed to consist of lodged sediment as due to numerous small water bodies or cavities at the ice bed interface. Aside from landform crests, no such peaks (bulk relative dielectric permittivity >10) were observed for the area assumed to consist of deforming sediment (e.g., 7–7.8 km), leading to the interpretation, that the sediment and ice are in direct contact and lack a significant thickness of water between.

2.2.2. Seismic Reflection Data

A seismic reflection profile (Smith & Murray, 2009; Smith et al., 2007), with length of 3.6 km and midpoint spacing of 5 m was acquired in 2004/05, two weeks prior to the airborne radar data. The dominant frequency of the seismic data set is ~150 Hz. Acoustic impedance of subglacial material along the profile was calculated following Smith (1997b), including the corrected attenuation factor of Holland and Anandakrishnan (2009). Acoustic impedances of crystalline bedrock can exceed 16 × 10^6 kg m^{-2} s^{-1} (Salisbury et al., 2003), but lies at 3–11 × 10^6 kg m^{-2} s^{-1} for sedimentary rock (e.g., sandstone (Gardner et al., 1974)). The lower end of this range overlaps with values for poorly lithified sandstone or compressed sediment (therefore low density and high porosity). Acoustic impedance can be used to differentiate between non-deforming and deforming sediment (Atre & Bentley, 1993; Smith, 1997a). Following Muto et al. (2019), we assume acoustic impedance of >3.8 × 10^6 kg m^{-2} s^{-1} to be associated with lodged (non-deforming) sediment and a porosity of ≤0.3 (Atre & Bentley, 1993; Muto et al., 2019). Shear stress is assumed to cause an increase in porosity due to dilation to around 0.4 (Atre & Bentley, 1993; Boulton, 1976; Boulton & Dent, 1974; Boulton et al., 1974). The acoustic

impedance of soft, water-saturated sediment that is deforming is ~2.3–3.8 × 10^6 kg m^{-2} s^{-1}. Corresponding ranges of till porosity presented in Figure 2 are taken from Atre and Bentley (1993). The acoustic impedance of water is ~1.5 × 10^6 kg m^{-2} s^{-1} (cyan line in Figure 2). The maximum error in the acoustic impedance for RIS using this approach is estimated to be ±0.5 × 10^6 kg m^{-2} s^{-1} (Smith, 1997b).

Acoustic impedance measurements suggest that the region from 6.5–7.9 km (Figure 2) consists of sediment with high porosity (>0.45), similar to the Bump (8.4 km) and MSGL 3 (9.1 km) which consist of deforming sediment (porosity ≥0.4). The high impedance at 8 km implies a more compressed sediment compared to the surrounding area. The only area where acoustic impedance implies a very compressed sediment (porosity much less than 0.3), possibly poorly lithified rock, is from 9.4–9.8 km.

3. Methods

3.1. Calculation of Bed-Reflection Power (BRP) of Surface Radar Data

Data presented here have been bandpass filtered (2–10 MHz passband), and amplitudes corrected for geometric spreading losses. Profiles are 2D migrated (using a finite difference approach and migration velocity of 0.168 m ns^{-1}), after which the bed reflection is picked using ReflexW software (Sandmeier Scientific Software). The received power P is calculated following Gades et al. (2000)

$$P \equiv \frac{1}{2(t_2 - t_1 + 1)} \sum_{t_1}^{t_2} A_i^2 \quad (1)$$

where A_i are the amplitudes within the time window t_2–t_1 centered on, and encompassing, the bed reflection (here, a 280 ns time window is chosen, corresponding approximately to one period of the 3 MHz wavelet). The amplitude of the received power is dependent on geometric losses, attenuation within the ice column and the properties at the ice-bed interface. System effects are neglected since the coupling between the antennas and the surface is assumed constant and system parameters are fixed over the period. The effect of englacial attenuation and scattering of the energy are the greatest source of uncertainty when analyzing the received power from the bed and will be discussed in the following sections.

3.1.1. Bed Roughness Effects (Scattering)

Increased bed roughness results in enhanced scattering of reflected energy and therefore reduced amplitudes of nadir reflected energy (Ulaby et al., 1982). Effects of roughness on reflectivity will be most sensitive at a scale comparable to the radar wavelength in ice (Grima et al., 2012), which is 56 m for the surface radar data in this study.

To estimate the roughness of the RIS bed along our profile, we calculated RMS-height along the airborne radar line (Murray et al., 2008, Figure 2) following MacGregor et al. (2013) and Cooper et al. (2019). Roughness is calculated within a 28 m window, consistent with the diameter of the migrated Fresnel zone of the surface radar data. The RMS-height of the de-trended data (remaining topography wavelength <28 m) is below 0.4 m. MacGregor et al. (2013) show that, at this scale, the decrease in reflectivity on 2 MHz data due to roughness effects is negligible. Differences in sensitivity of the 2 MHz (as in MacGregor et al., 2013) and 3 MHz (this study) wavelet to roughness on this scale is negligible. We therefore assume the effect of roughness on reflectivity to be negligible in this study.

3.1.2. Effects of Varying Ice Thickness (Englacial Attenuation)

Matsuoka (2011) demonstrated that the attenuation rate can vary significantly over distances of 120 km, suggesting that attenuation rates should be calculated using estimates of ice temperature and chemistry. At RIS we have no data to constrain information about variations in chemistry or the temperature of the ice on the <20 km scale of this study. Furthermore, Ashmore et al. (2014) recommended the assumption of a uniform englacial attenuation to be appropriate for small regions, assuming unchanging englacial properties, and this is the approach we use.

Losses due to englacial attenuation and geometric spreading should both be a smooth function of the ice thickness (Gades et al., 2000). We therefore fit an exponential decay function (lines in Figure S1a in Supporting Information S1) to the received power versus two-way travel time pairs (black dots). This fitted function, called BRP_{est}

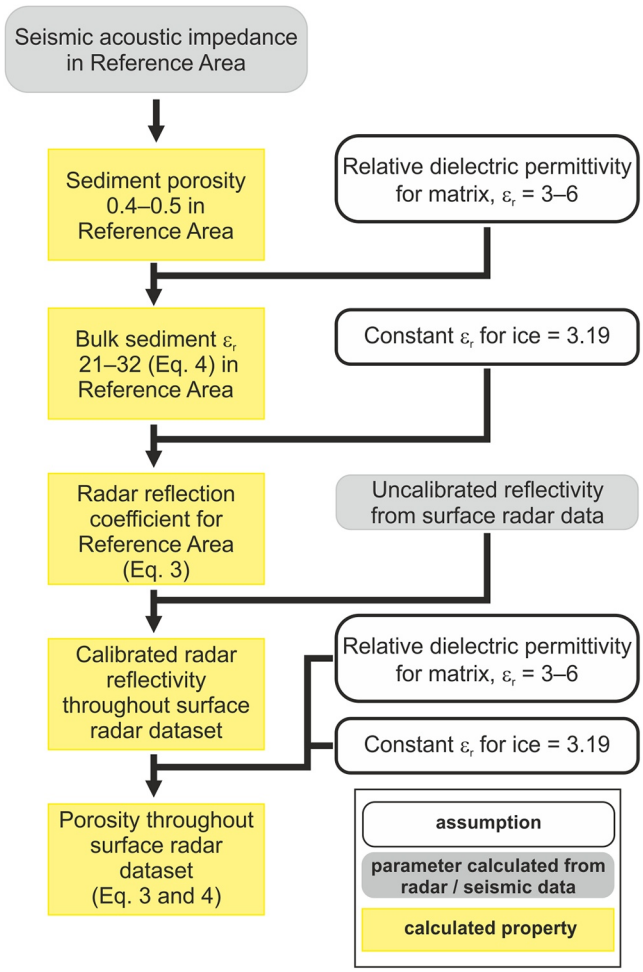

Figure 3. Calibration routine applied to surface radar data: Sediment porosity inferred from seismic acoustic impedance is used to calculate the reflection coefficient in the Reference Area. The reflection coefficient in the Reference Area is then used to calibrate the reflectivity within the Reference Area and along the whole data set. From the calibrated reflectivity, spatial variation in sediment porosity can be calculated.

describes the variation in power, solely due to variations in ice thickness (depth averaged attenuation rate corresponding to ~20 dB/km). The final BRP is calculated as (Gades et al., 2000)

$$\mathrm{BRP} = \frac{P}{\mathrm{BRP}_{\mathrm{est}}}. \tag{2}$$

The BRP, as defined here, is a measure of the power reflected at the bed, corrected for ice thickness variation (Chu et al., 2016; Jacobel et al., 2010).

To estimate the validity of a uniform attenuation rate we analyzed the internal power reflected from the ice column (as an index of englacial attenuation (Catania et al., 2003; Gades et al., 2000)) within a time window that spans from 500 ns below the airwave until 500 ns above the shallowest point of the bed reflection. Measured englacial reflected power is constant along flow, however an increase in englacial reflected power can be seen towards the Ellsworth Mountains (Figures S1 and S2 in Supporting Information S1). Nevertheless, we use the whole data set when analyzing the depth averaged attenuation BRP_{est} based on received power from the bed (similar to Bentley et al., 1998; Gades et al., 2000; Jacobel et al., 2009; Winebrenner et al., 2003) to allow a wide range of ice-thickness. The latter was emphasized by Schroeder et al. (2016), who found that using segments of the data to analyze effects of attenuation can improve the spatial resolution however, at the expense of resolution they suggested that segments should consist of data with sufficient topographic relief. To account for observed lateral variations in englacial attenuation across our study region we introduce uncertainty bounds to the BRP and therefore calculated reflectivity (±0.15 V, Figure 5b). This uncertainty is calculated based on variation in englacial attenuation measured with subsets of the data across the region.

The resulting BRP is proportional to the square of the reflection coefficient R, which we can use to infer bed properties. In the following the term reflectivity is referred to $\sqrt{\mathrm{BRP}}$ in volts. However, it is important to note that the estimates of reflectivity that we obtain here are not absolute, but instead are relative indicators of reflection strength.

3.2. Calibration of the Reflectivity

If a control point with known dielectric contrast is available (e.g., an ice-water interface at the base of an ice shelf), recorded amplitudes can be expressed as absolute reflectivity (e.g., Murray et al., 2008) and, thus, the bulk relative dielectric permittivity for the subglacial material can be calculated. As surface radar data acquired in 2016/17 do not include the reflection of the base of an ice shelf, a different approach to calibrate the reflectivity is taken in this study, where bed properties of the control point are inferred from previous studies. The underlying principle of both approaches is similar, where assumed properties in an area are used to calculate the reflection coefficient, which is then used to calibrate the reflectivity along the whole data set (Figure 3).

3.2.1. Reflection Coefficient

Most studies assume low-loss conditions, where the contribution of electrical conductivity to reflectivity can be neglected, although Tulaczyk and Foley (2020) show that this may not be valid where clay-rich material and/or saline pore water is present at the glacier bed. Our interpretation neglects electrical conductivity effects, but the validity of this assumption is revisited in later discussion.

Assuming that bulk relative dielectric permittivity of the glacier bed and the overlying ice is known in at least one location (the so called "Reference Area" defined in Section 3.2.3), the reflection coefficient can be calculated as

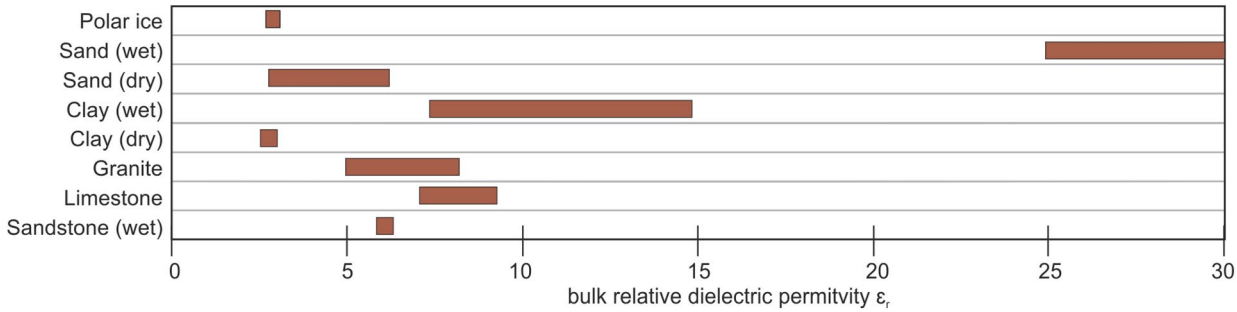

Figure 4. Bulk relative dielectric permittivity for different materials (values taken from Daniels (1996); Davis and Annan (1989); Martinez and Byrnes (2001); Reynolds (1997)).

$$R = \frac{\sqrt{\varepsilon_{r1}} - \sqrt{\varepsilon_{r2}}}{\sqrt{\varepsilon_{r1}} + \sqrt{\varepsilon_{r2}}} \tag{3}$$

where ε_{r1} and ε_{r2} are the bulk relative dielectric permittivity above and below the interface, respectively (Martinez & Byrnes, 2001). Here we assume ε_{r1} corresponds to ice (3.19; Fujita et al., 2006; Martinez and Byrnes, 2001), and ε_{r2} to subglacial material. The bulk relative dielectric permittivity measured for wet sand ranges with varying water content 10–30 (Daniels, 1996; Davis & Annan, 1989), and for dry sand from 3–6 (Reynolds, 1997, Figure 4). We can exclude the potential of a phase change of the reflection coefficient and therefore a change in phase of the reflection as we are not expecting the material below the ice to contain a lower bulk relative dielectric permittivity than ice. Furthermore, no polarity changes have been observed for the bed reflection in the radar data.

The reflection coefficient calculated for the Reference Area can then be used to calibrate the reflectivity along the entire surface radar data set, as changes in the reflectivity, therefore amplitude of the reflection, are proportional to changes in the reflection coefficient. Assuming uniform ice properties over the area (as assumed when correcting for attenuation), the bulk relative dielectric permittivity of subglacial material can be calculated for all points along the surface radar track following Equation 3.

3.2.2. Bulk Relative Dielectric Permittivity and Porosity

The bulk relative dielectric permittivity of rocks and sediments depends on the individual relative dielectric permittivities of mineral grains and pore fluid, plus pore geometry and pore water fraction (Martinez & Byrnes, 2001), and there are different mixing models by which these elements are combined. Following Mount and Comas (2014) and Martinez and Byrnes (2001) we calculate the bulk relative dielectric permittivity ε_r of a material with varying porosity ϕ as

$$\varepsilon_r = \phi S_w \epsilon^{\alpha}_{r(\text{water})} + (1-\phi)\epsilon^{\alpha}_{r(\text{matrix})} + \phi(1-S_w)\epsilon^{\alpha}_{r(\text{air})} \tag{4}$$

where $\varepsilon_{r(\text{water})}$, $\varepsilon_{r(\text{matrix})}$ and $\varepsilon_{r(\text{air})}$ are the relative dielectric permittivity of water ($\varepsilon_r = 80$), (dry) matrix and air ($\varepsilon_r = 1$), respectively. S_w is water saturation, which we assume to be 100%, hence $S_w = 1$ and terms related to air are neglected. The geometric factor α (ranging between -1 and 1) relates to the orientation of the electrical field compared to the geometric arrangement of mixture constituents of the material (Knoll, 1996). A value of 0.5 was found to be appropriate for most geologic materials (Roth et al., 1990) and following Mount and Comas (2014) and West et al. (2003) we adopt $\alpha = 0.5$. This model and the available data mean that the bulk relative dielectric permittivity is sensitive to variations in porosity and different matrix compositions, but neglects effects such as mixture of minerals in the matrix, grain/pore geometry and grain-grain contacts. Notwithstanding these limitations, changes in reflectivity can therefore be linked to changes in porosity and matrix composition. Figure 5 shows how the reflection coefficient varies with porosity, for matrix materials with a range of relative dielectric permittivity. Each individual line assumes a constant relative dielectric permittivity for the matrix, resulting in a bulk relative dielectric permittivity. Values of relative dielectric permittivity of the matrix are chosen to represent dry sand and pore spaces are assumed to be 100% water filled. Nevertheless, only the bulk relative permittivity at 0 porosity does represent dry sand, as the bulk relative permittivity changes with varying porosity.

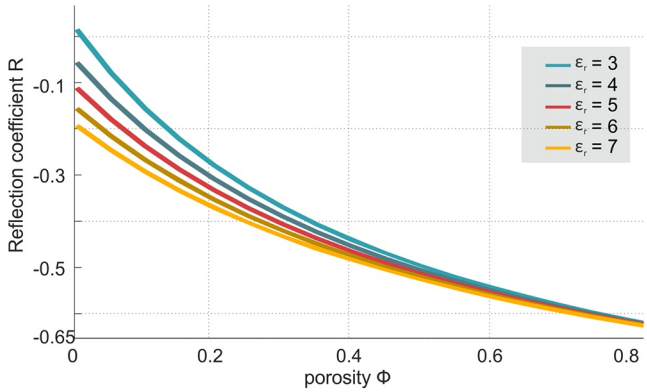

Figure 5. Variation of reflection coefficient with porosity according to Equations 3 and 4, for water-saturated sediment with different matrix permittivities overlain by ice. Matrix permittivity values are taken from Daniels (1996), Davis and Annan (1989), Martinez and Byrnes (2001). Only the bulk relative dielectric permittivity at 0 porosity represents dry sand, as the bulk relative dielectric permittivity changes with varying porosity (assuming all pore space to be filled with water).

3.2.3. The Choice of a Reference Area

Spatial variations in porosity inferred from variations in reflection coefficient from Equations 3 and 4 are highly dependent on the reliability of the properties chosen for the Reference Area. Therefore, the Reference Area for calibration was chosen along surface radar line 1007, which is intersected by both the airborne radar and seismic line (Figure 1c). Furthermore, this is approximately the location of the 2018/19 drilling campaign (Smith et al., 2020). Drilling accessed the bed, however sediment samples retrieved have not been fully analyzed yet, but further validation of the results of this study might be possible in the future.

In general, acoustic impedance should decrease with increasing porosity since water typically softens a material, while radar reflectivity would increase (due to increasing water content and the stronger dielectric contrast with the overlying ice). However, a direct comparison between acoustic impedance and radar reflectivity is not trivial, as impedance describes properties of a layer, while the reflectivity is a property of the boundary of two layers. In our case, we assume the properties of the upper layer, which represents ice, not to be changing, therefore changes in the surface radar reflectivity are a proxy for changes in dielectric permittivity of the underlying material and therefore the electromagnetic impedance. However, as the surface radar reflectivity is not calibrated, no absolute values of electromagnetic impedance can be calculated. Acoustic impedance is high for sedimentary rock (3–11 $\times$ 10^6 kg m^{-2} s^{-1} (Gardner et al., 1974)) or crystalline rock (>16 $\times$ 10^6 kg m^{-2} s^{-1} (Salisbury et al., 2003)) and will result in a stronger seismic reflection, where the theoretical radar reflectivity shows only little difference between a sand of low porosity (R = 0.01 to −0.11, $\varepsilon_{r(\text{matrix})}$ = 3–5) and a sandstone (R = −0.11 to −0.27, $\varepsilon_{r(\text{wet sandstone})}$ = 5–10), or a granite (R = −0.19, $\varepsilon_{r(\text{wet granite})}$ = 7). This relationship is reversed when a water layer of sufficient thickness is present. The acoustic impedance of water is low (~1.5 $\times$ 10^6 kg m^{-2} s^{-1}), whereas the sensitivity of radar waves to water (R = −0.68, $\varepsilon_{r(\text{water})}$ = 80) is much higher when compared to seismic. Figure 6 shows values of surface radar reflectivity and acoustic impedance along a part of surface radar line 1007. Low acoustic impedance values, interpreted as soft sediment (6.5–7.9 km, Bump and MSGL 3) are calculated in areas of high surface radar reflectivity. Low surface radar reflectivity is observed where high acoustic impedance indicates a very low porosity material (e.g., 8 and 9.6 km). However, no empirical relation to convert acoustic impedance to radar reflectivity exists. The acoustic impedance and surface radar reflectivity beneath RIS show a poorly constrained linear relation with a negative slope (Figure S3 in Supporting Information S1). Due to the lack of a clear correlation between acoustic impedance and radar reflectivity (Figure S3 in Supporting Information S1), surface radar data can not be calibrated using the whole length of the seismic profile but needs to be limited to an area, where porosity estimates from acoustic impedance can be used to calculate the radar reflection coefficient. The location of the Reference Area should therefore first be limited to an area, where the bed does not consist of consolidated sediment or bedrock, and second should be an area where we expect no liquid water to be present, but where the bed is expected to consist of soft sediment. Concerning the first restriction, this rules out most of the seismic line between 8.5–10 km. The second rules out the crest of landforms, where the presence of liquid water has been interpreted from airborne radar data (Murray et al., 2008). Finally, the area used for the calibration is between 6.5–7.9 km (marked by the red line in Figure 6). This area along surface radar line 1007 is now referred to as Reference Area.

3.2.4. Bed Properties in the Reference Area

Acoustic impedance in the Reference Area varies between 1.66 and 2.38 $\times$ 10^6 kg m^{-2} s^{-1}, implying soft sediment. To account for uncertainties arising from the analysis of acoustic impedance, we assign a porosity of 0.4–0.5 to the Reference Area. We have no further information on the properties (relative dielectric permittivity) of the matrix material and therefore assign a range of relative dielectric permittivity of 3–6 consistent with dry sand (Figure 4). The resulting bulk relative dielectric permittivity in the Reference Area for sediment with 0.4–0.5 porosity therefore ranges between 21–32. This range of material properties is assigned to all reflectivity values calculated for the Reference Area, encompassing the uncertainties arising from the correction of englacial attenuation (see

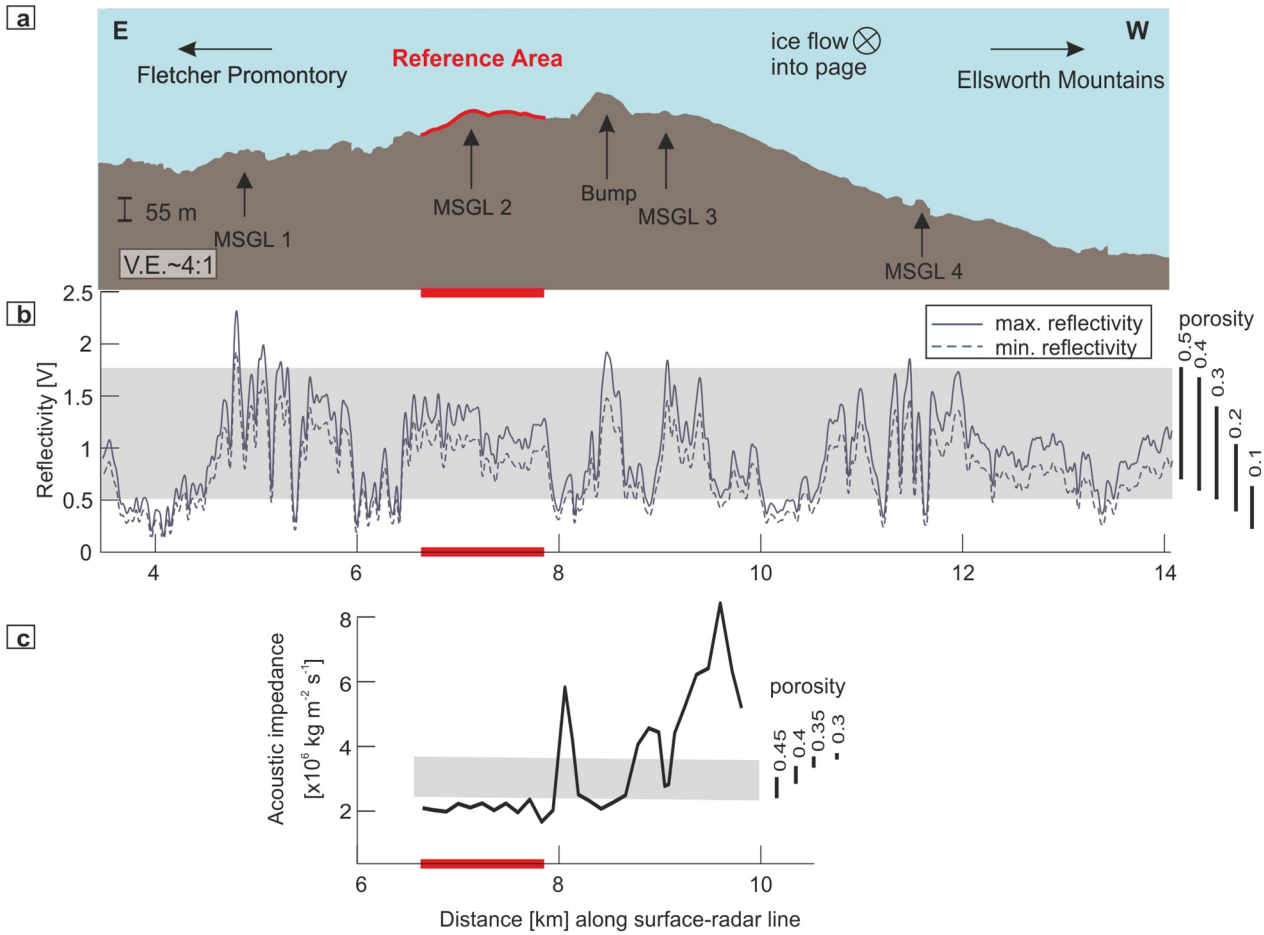

Figure 6. Surface radar reflectivity compared to seismic acoustic impedance. (a) Bed topography along parts of line 1007 (see red arrow in Figure 1c), interpreted from surface radar; ice flows into the page. (b) Surface radar reflectivity along line 1007. Reflectivity as shown here is uncalibrated and therefore expressed as the dimensionless ratio of voltage. Vertical bars at the right show calculated porosities according to variations in reflectivity compared to the Reference Area (red line at 6.5–7.9 km). (c) Acoustic impedance along line C1_04, with possible porosity ranges (Smith & Murray, 2009). The gray box in (b) and (c) show values of 2.2–3.8 × 10^6 kg m^{-2} s^{-1}, corresponding to soft, deformable sediment. The whole profile of line 1007 of surface radar data is displayed in Figure S4 in Supporting Information S1. Ranges of reflectivity assigned to values of porosity are listed in Table S1 in Supporting Information S1.

Figure 6b). The reflection coefficient in the Reference Area can now be used to calibrate the calculated reflectivity and therefore infer porosity through the whole data set, assuming invariant matrix dielectric properties and constant properties of the overlaying ice (Figure 3). The resulting ranges of reflectivity assigned to a certain value of porosity are listed in Table S1 in Supporting Information S1. By assigning a range of relative dielectric permittivity (3–6) to the matrix material, we allow spatial variations in matrix composition (additional to variations in porosity). While we cannot exclude temporal changes in bed properties, no temporal changes in seismic acoustic impedance were identified from repeated seismic surveys (Smith & Murray, 2009; Smith et al., 2007) within the Reference Area and seismic profiles are highly repeatable over several years, which implies bed properties are likely to be stable.

4. Results

4.1. Spatial Variation in Surface Radar Reflectivity

The spatial variation in reflectivity calculated from 2016/17 surface radar data (Figure 7) shows a preferred orientation in the flow direction in the area of deforming bed (upstream of boundary (King et al., 2009), average reflectivity = 0.9 V). High reflectivity values (>1.5 V) are aligned in thin bands in the ice flow direction. These reflectivity patterns are consistent over lengths of 14 km, and may exceed the length of the acquired grid. The

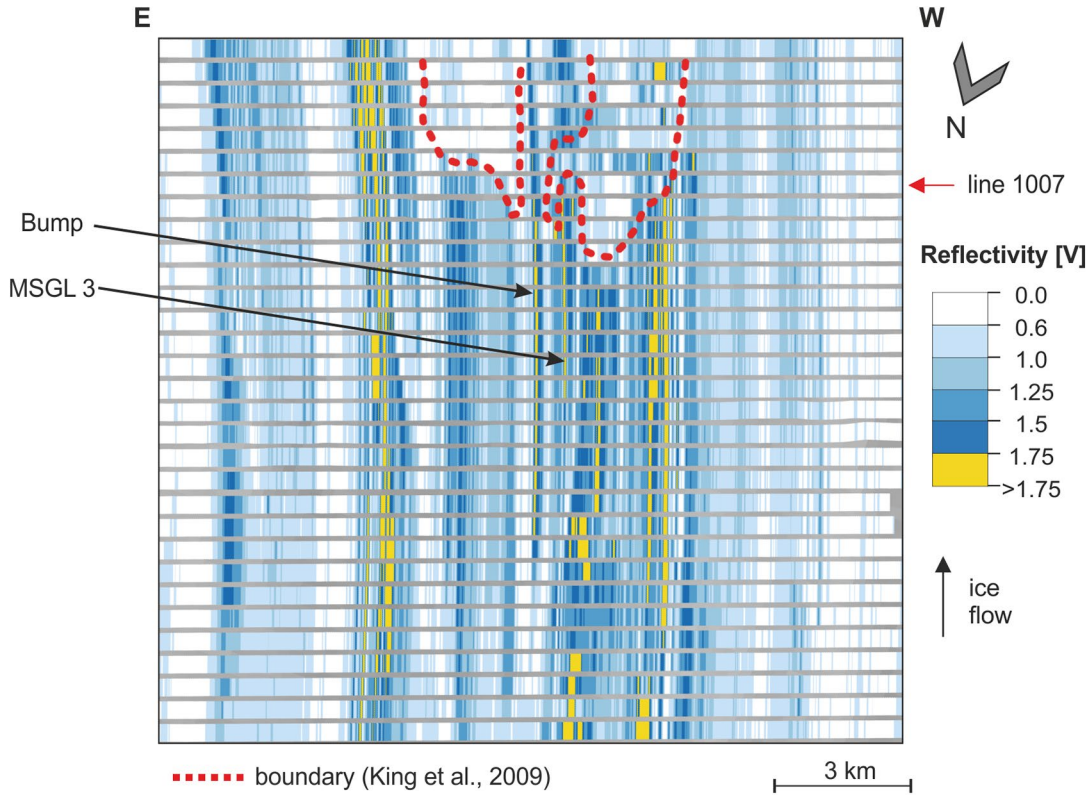

Figure 7. Surface radar reflectivity, corrected for ice thickness variation. Location of grid given in Figure 1c. The deep valleys of the bed are located on the left (eastern valley) and the right (western valley) of the image. The sediment downstream of the red dashed boundary is assumed to be stiff till (basal sliding), opposing to the soft sediment (deforming bed) upstream of the boundary.

reflectivity is low in the area of basal sliding, downstream of the boundary (King et al., 2009), with average reflectivity = 0.7 V.

The bed topography (Figure 8) shows the asymmetric valleys to the east and west of a central ridge, with the valleys associated with lower reflectivity than the ridge. The bed is characterized by many elongated landforms (elongation-ratio between 1:20 and 1:100). The most prominent one, the Bump (Smith, 1997b; elongation-ratio 1:28) lies in the center of the image. Superimposing the reflectivity on the bed topography shows thin bands of high reflectivity aligned with ice flow, in some areas located at the crest of landforms, whereas the troughs around the landforms show low reflectivity (darker colors on the crest compared to the lighter troughs in Figure 8).

The spatial variation of reflectivity across flow (in acquisition direction) varies on a scale of ~200 m (Figure 6). The highest reflectivity received was 2.3 V at 4.8 km, the lowest was 0.16 V at 1 km (Figure S4 in Supporting Information S1). Peaks in reflectivity are in some areas located on the crest of landforms (e.g., at distance 4.7, 4.9, 5.0, 8.4, 9.0, 11.1, and 14.6 km (Figures 6 and 8)). Landforms in the western valley seem topographically less pronounced and show a lower reflectivity when compared to landforms on the central ridge.

4.2. Spatial Variation in Porosity Based on Surface Radar Reflectivity

The calculated porosity along line 1007 is shown in Figure 6b as vertical bars. For most of the areas along the surface radar line, modeling results in porosities of deforming sediment (~0.3–0.5), with lower porosities (<0.3) around km 4, 6–6.5, 8–8.4, 8.7, 9.5, 10. Consistent with modeled porosities from surface radar reflectivity, acoustic impedance in the area around 8 km suggests porosities below 0.3, similarly at 8.8 and 9.5 km. Sediment with porosity higher than 0.5 are indicated for areas around 4.7, 5, 5.2, 8.4, 9, 11.4 km (Figure 6), while acoustic impedance around 8.4 and 9 km suggests porosity of around 0.45.

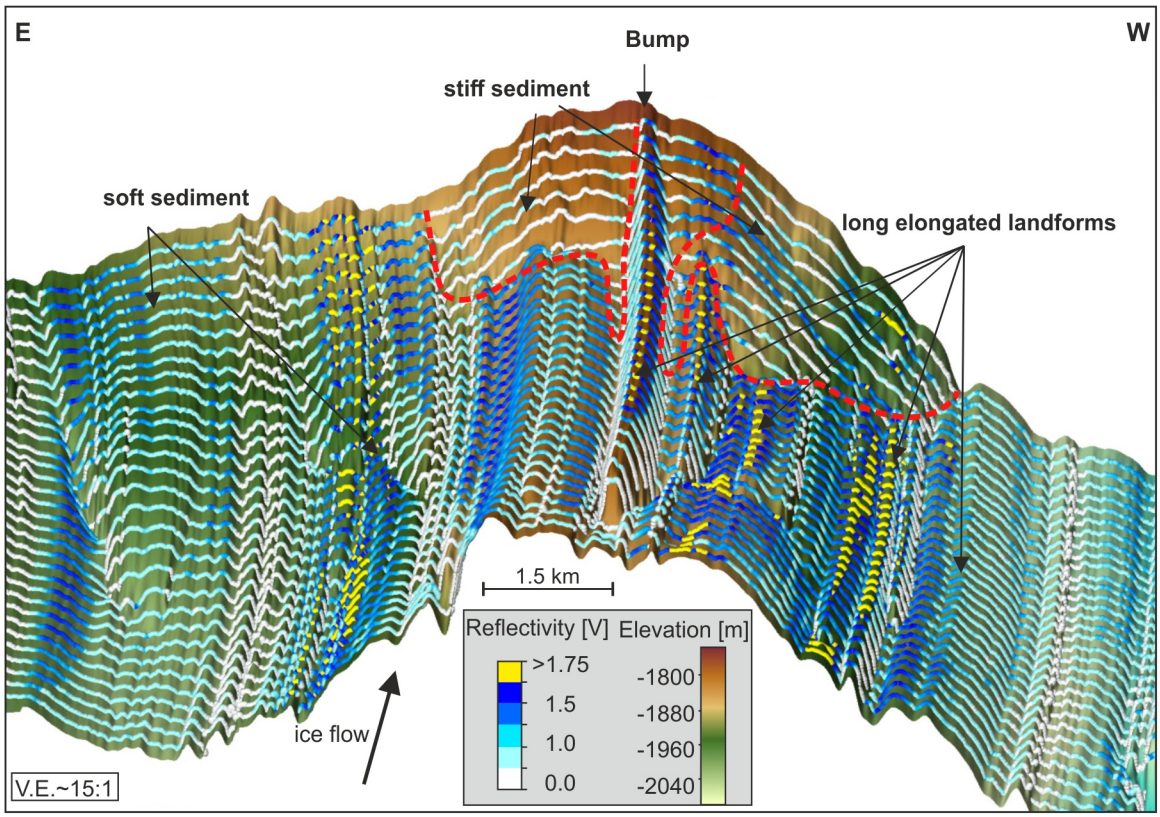

Figure 8. Bed elevation (referenced to WGS84 ellipsoid), interpolated onto a surface with 50 × 20 m grid cells. Ice flow is into the page, parallel to elongated landforms. The prominence of these is exaggerated for display, with vertical exaggeration (V.E.) of ~15:1. The lines perpendicular to ice flow represent reflectivity along the surface radar tracks (color similar as in Figure 7).

4.2.1. High Reflectivity and Water

High values in surface radar reflectivity at 8.4 and 9 km coincide with values of high bulk relative dielectric permittivity in airborne radar data, interpreted as liquid water by Murray et al. (2008). Although most other areas of high surface radar reflectivity are co-located with higher bulk relative dielectric permittivity derived from the airborne data, none is sufficiently high to indicate liquid water but possibly related to small water ponds with sub-resolution thickness (quarter of the airborne radar wavelength in water ($\lambda \approx 0.034$ m s^{-1}/150 MHz = 0.226 m), that is, maximum water depth <0.056 m). The high bulk relative dielectric permittivity at 6.8 and 9.4 km from the airborne data (Figure 2) is located in an area of high surface radar reflectivity, although modeled porosities in this region are in the range of deforming sediment.

4.2.2. Properties of Subglacial Landforms

Some landforms identified on the bed are associated with high surface radar reflectivity for example, the Bump, MSGL 1, MSGL 3 and MSGL 4. The reflectivity along the crests of some landforms tends to increase around 2–2.5 km downstream of their upstream end (Figure 9c), while the upstream end of the landform shows a low reflectivity (upstream of line 1026), indicating a lower porosity material. However, only two upstream ends of landforms (Bump and MSGL 3 (Figure 9)) are recorded within this study. Downstream of the increase in reflectivity, the landforms retain their high reflectivity until they terminate (Figures 8 and 9). The reflectivity of the landforms flank is lower when compared to the crest (Figure 9a), furthermore, the trough present around some landforms shows a sufficiently low reflectivity to indicate low porosity material (Figures 9b and 9c).

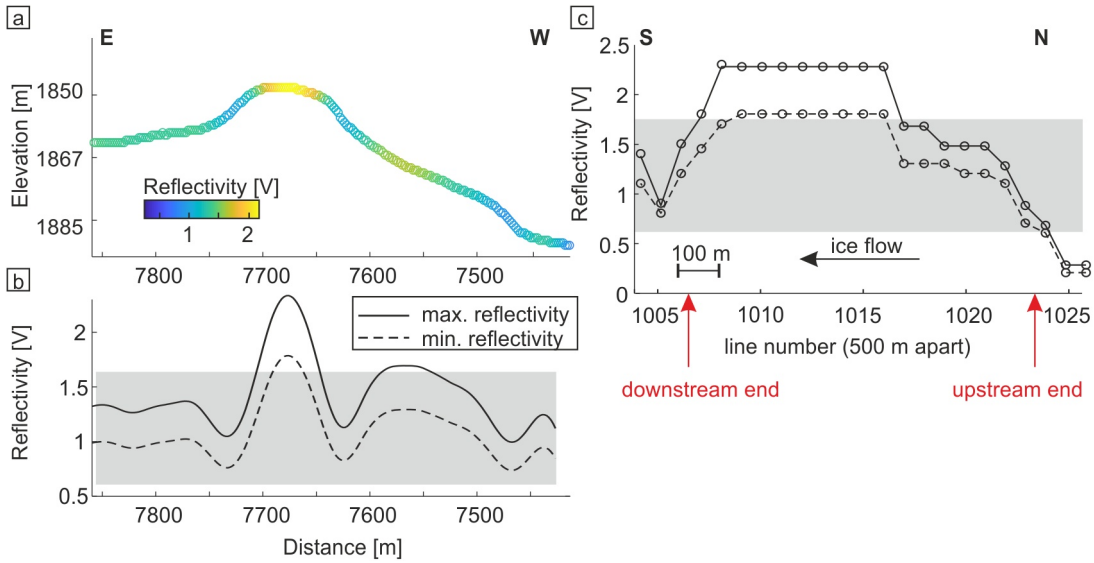

Figure 9. Reflectivity of MSGL 3. (a) Bed elevation (referenced to WGS84 ellipsoid) along line 1013, which is located 300 m upstream of line 1007 shown in Figure 6. Color coding represents the reflectivity, as also seen in (b). (c) Reflectivity along the crest and further upstream in line with the crest of MSGL 3. The gray box in (b) and (c) show values corresponding to soft, deformable sediment (see Figure 6).

5. Discussion

5.1. Bed Properties

Calculated porosities on the bed indicate the presence of soft sediment (porosity ~0.3–0.5) as well as low porosity material (porosity <0.3). The reflectivity calculated for some landform crests suggests porosities of more than 0.5. Porosities of subglacial till recovered from different locations vary between 0.2–0.6 (Evans et al., 2006; Kamb, 2001). Sediment with porosities higher than this are less likely to occur in the subglacial environment due to the compression of the overlying ice (vertical stress ~20 MPa). Due to this, the high reflectivity (>1.78 V) observed under RIS (Figures 7 and 8) cannot solely be explained by changes in sediment porosity, and additional sources of reflectivity must be involved. Comparisons of surface radar data and interpretation of airborne radar data (Murray et al., 2008) suggest the high reflectivity signals, for example, on the crest of some MSGLs, are likely to be caused by water overlying soft sediment. Further implications of this are discussed below.

Spatial variations in reflectivity (Figure 7) within the deforming and sliding bed indicate that the subglacial material is not homogeneous within these areas, which is consistent with the variations seen in bulk relative dielectric permittivity from airborne radar data (Figure 2). Due to a big overlap of porosities calculated for a certain range of reflectivity Figure 6b and Table S1 in Supporting Information S1 a differentiation of porosities within the range of deforming sediment (porosity = 0.3–0.5) is not possible.

5.2. Low Porosity Material

Modeling results derived from the surface radar reflectivity indicate the existence of porosities less than 0.3 (e.g., around km 4, 6, 8, 8.7, 10). Such low porosities can indicate a very compressed unlithified sediment or a sedimentary rock. However, using the modeling results we are only able to make assumptions about the porosity, but cannot infer anything about consolidation stages or different rock types solely from surface radar data. Seismic acoustic impedance calculated for the bed of RIS are as high as 8×10^6 kg m^{-2} s^{-1} (Figure 6c), therefore suggesting a sedimentary rock, like sandstone, rather than a crystalline basement.

The sediment under RIS is interpreted to be water-saturated and at the pressure-melting point (Smith et al., 2020; Smith & Murray, 2009). Nevertheless, an alternative interpretation of these low values in reflectivity coinciding with higher values in acoustic impedance (Figure S3 in Supporting Information S1) might be the existence of a frozen substratum in parts of the bed. This is considered less likely but has not been critically reviewed so far. The observed pattern of acoustic impedance variations could in principle be explained by a partly frozen pore

space as well as the occurrence of consolidated material or sedimentary rock, because a clear differentiation of the three cannot be made from the acoustic impedance (Smith et al., 2018). A reliable statement on whether there are frozen patches, or a low porosity material present is only possible combining several observations and methods. The fast and stable ice flow (Gudmundsson, 2006; Gudmundsson & Jenkins, 2009; Murray et al., 2007; Vaughan et al., 2008), the lack of significant spatial changes in basal drag at least at large scales over this area (Joughin et al., 2006), the occurrence of liquid water (Murray et al., 2008) and the correspondence of high acoustic impedance values to the very low surface radar reflectivity leads us to the interpretation that areas of very low reflectivity are most likely caused by low porosity material, either consolidated sediment or sedimentary rock.

5.3. Landforms and Water

High porosities, indicating soft sediment, are preferentially associated with some of the elongated landforms, while the troughs and the upstream end of the landform consist of lower porosity material, with no indication of free water. Analysis of their elongation ratio classifies the landforms upstream of the boundary as MSGLs, rather than drumlins (Everest et al., 2005; King et al., 2009). Those MSGLs are assumed to be depositional rather than erosional features (Smith et al., 2007) and therefore a material difference between the landforms and their surroundings is plausible and has been identified in other places (Barcheck et al., 2020). In both the surface and the airborne radar data (Murray et al., 2008), we have identified water occurring at the crest of some MSGLs (Figures 8 and 9) extending downstream for up to 10 km, until the downstream end of the landform is reached. Landforms consisting of a hard upstream end and a soft tail and downstream side have been described before by Clyne et al. (2020). Furthermore, Holschuh et al. (2020) and Clyne et al. (2020) described troughs around and at the upstream end of bumps to consist of hard material, which is consistent with the observations of this study.

Typical analyses of the subglacial hydraulic potential (e.g., Vaughan et al., 2008) would suggest free water is more likely to be present in the deeper valleys rather than on the central ridge, similarly in the troughs around landforms rather than the crest of landforms, due to the low surface slopes compared to the bed slopes (Smith et al., 2007). However, such analyses cannot account for smaller-scale and local conditions and processes and hence do not contradict our interpretations of water on landform crests. Several studies document evidence for water on landforms. McCabe and Dardis (1994) used sediment analysis to show that a drumlin in Ireland had a canal on its crest, as well as a lee-side cavities. Riverman et al. (2019) found two wet subglacial bedforms under North East Greenland Ice Stream, but with no evidence for a link between the water movement and the landform development. Clyne et al. (2020) interpreted water pockets on soft lee side bumps with a length of over 400 m and a depth of less than 2–6 m.

Subtlety in the basal topography at the landforms possibly create spatial small-scale variation in pressure and therefore the hydraulic potential across the profile of the MSGL, possibly driving locally produced (by compression of soft, water-saturated sediment or basal melting) water towards their crest rather than the flanks. Depending on the permeability of the sediment, these pressure variations may then result in the formation of a water body at the crest of some landforms. Assuming the landforms to consist of permeable material, whereas the surrounding area is less permeable material, the water on the landforms might get trapped on the crest, as water possibly cannot (or can only slowly) drain through the underlying material. This might be an important phenomenon, considering that downstream ends of landforms are often located in an area of low porosity. Water flow through that material might be inhibited, creating an accumulation of water on the landforms.

5.3.1. Geometry of Water Bodies Beneath RIS

The appearance of the high reflectivity in adjacent surface radar lines enables an estimate of the length as well as width of these water bodies. For the Bump and the MSGL 3, the signals are visible over a length of 8 and 4 km along the ice flow and width of 100 and 50 m across the ice flow, respectively. Other landforms show this pattern over a length of up to 10 km, with a width of up to 100 m.

The observations of water overlying the sediment is consistent with the water bodies interpreted as canals by Murray et al. (2008). Other studies have used additional evidence to differentiate between canals (cut into subglacial material) and channels (cut into the ice) (Schroeder et al., 2013). However, we have no additional information on the geometry of the water body to differentiate between a canal or channel. Nevertheless, the width of these water bodies suggests a broad waterbody, consistent with canals. One potential reason for the consistency of the high values in reflectivity along the crest of landforms is a hydrological linked system, rather than individual, not

connected water ponds. However, we cannot make any statement about these water bodies being part of a water evacuation system because in our study area these water bodies do not have any obvious sink or source, and there is no indication of water beyond the end of the landform (e.g., around the boundary or in the lee of landforms).

Indications for liquid water on the bed of RIS in most places is present in both radar data sets, although the intensity of the signal varies between the airborne and surface radar data. We cannot exclude that these high reflectivity signals, indicating liquid water, are a transient signal and the amount of water available might change overtime, and therefore explains differences seen between airborne and surface radar data. However, signals of water on the Bump and MSGL 3 are present in both surveys, indicating temporal consistency in spatial distribution.

5.4. High Reflectivity and Electrical Conductivity

In glaciology, the interpretation of high reflectivity originating from water has typically been made by assuming the glacier bed to be a low-loss medium. However, Tulaczyk and Foley (2020) stated that reflections at an interface between ice and a material with high conductivity can appear as bright (high reflectivity) or even brighter than a reflection of a water body (e.g., subglacial lake) for low frequency radars (e.g., the surface radar in our study). Highly conductive subglacial materials causing such high reflectivity could be, for instance, clay-bearing sediments, materials including seawater- or brine-saturated sediments and bedrock (Foley et al., 2016). We cannot rule out the possibility that the bed in the areas of high reflectivity consists of a high-loss material. However, the frequency dependence of the reflectivity for different materials makes this less likely. The airborne radar data (∼150 MHz) will still be influenced by high conductivity but on a smaller scale compared to the surface radar data, therefore, the signals of these two radar data would be expected to differentiate under non low-loss conditions, which is not the case here.

5.5. Interpretation of Spatial Pattern of Bed Properties

Figure 10 presents our interpretation of the bed properties. According to this interpretation the bed of RIS partly consists of soft sediment (0.3–0.5 porosity). Elsewhere, low porosity material (<0.3 porosity) is present at the bed. Figure 10a suggests that the distribution of different materials is more complex compared to previous studies, where the upstream part of the study area was interpreted to entirely consist of soft sediment (King et al., 2009). Furthermore, we have shown that the boundary between soft sediment and low porosity material is more complex than previously defined by King et al. (2009).

Subglacial landforms consist of soft, water-saturated sediment (Smith & Murray, 2009; Smith et al., 2007), while the troughs around and towards the upstream end of some landforms consist of harder material. Water bodies located on the crest of some landforms are aligned in the flow direction over a length of up to 10 km. A prominent isolated region of free water is located in the area of sliding bed (Figure 10 see yellow square), within an area of softer sediment. We suspect a possible link between this isolated spot and the water bodies further upstream, as they are co-linear along the ice flow. The isolated spot appears to be the first location downstream of the landform consisting of soft sediment.

6. Conclusions

Surface radar data were collected on Rutford Ice Steam in a 15 × 17 km grid to constrain in situ bed properties over a wide spatial extent, including an area where previous surveys indicate spatial heterogeneities in bed properties. The uncalibrated surface radar reflectivity was combined with porosities inferred from seismic acoustic impedance to model sediment porosities along the grid. The combination of the high spatial coverage of the surface radar data and the constraints in bed properties from acoustic impedance enabled the interpretation of the distribution of bed properties over a wide area at a scale normally only considered in satellite or offshore studies of deglaciated areas.

Surface radar reflectivity indicates the existence of soft sediment as well as low porosity material at the bed of RIS. Highly porous sediments reduce the basal drag and facilitates fast ice flow. Bed properties within the pre-defined deforming and sliding bed (King et al., 2009) vary. Areas previously assumed to be dominated by sediment deformation partly show localized outcrops of low porosity material, indicating a combination of basal sliding

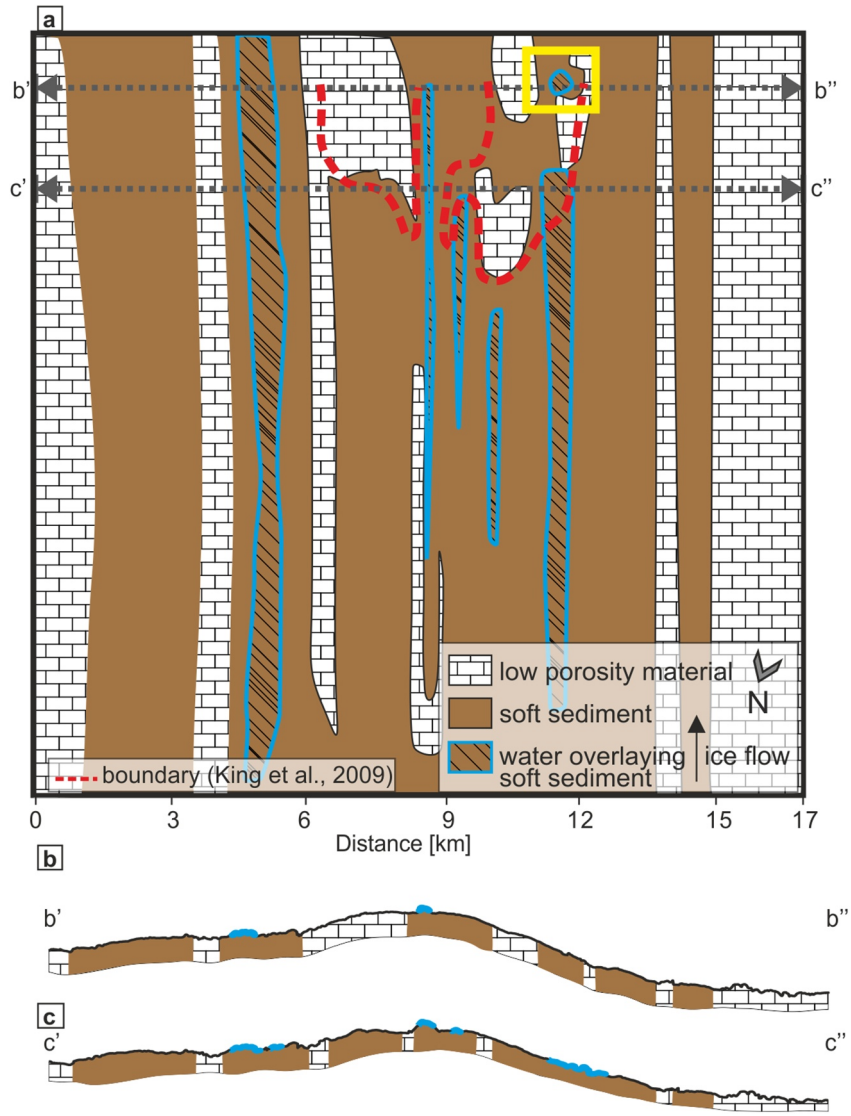

Figure 10. Conceptual model of the spatial pattern of bed properties under the RIS. (a) Plan view, including earlier lineation of the stiff/soft boundary. The yellow square marks a prominent isolated region of free water in the sliding area. (b) and (c) show cross-sections through the bed at surface radar line 1003 (b' to b'') and 1007 (c' to c''), although sediment depth is unconstrained.

and deformation in that area, consistent with the co-existence of a deforming and non-deforming stable bed in the palaeo record described as a mosaic-like pattern by Piotrowski and Kraus (1997) and Piotrowski et al. (2004).

The bed consists of numerous elongate landforms, classified by their elongation ratio as MSGLs, consisting of soft sediment (Smith & Murray, 2009; Smith et al., 2007). Both airborne and surface radar data indicate free water overlying sediment on the crest of some MSGLs, as well as an isolated spots. The water bodies show length of up to 10 km, with a maximum width of 100 m. The trough around landforms as well as the landforms upstream end consist of lower porosity material. The spatial variation of material properties, and therefore possibly permeability, may be the mechanism behind the occurrence of water on the crest of landforms, rather than in their trough. However, more observational work, together with modeling are necessary to analyze the water on the crest of landforms under Rutford Ice Stream more quantitatively.

Data Availability Statement

The data, which supported the main findings of this work (Power reflected from the bed reflection acquired using the surface radar data), are available via the UK Polar Data Centre (UK PDC): https://data.bas.ac.uk/full-record.php?id=GB/NERC/BAS/PDC/01438 (Schlegel et al., 2020).

Acknowledgments
R. Schlegel was funded by a Natural Environment Research Council (NERC) PhD Studentship through Swansea University (Project Studentship grant NE/G013187/1). This work was funded by NERC AFI award numbers NE/G014159/1 and NE/G013187/1. We thank BAS Operations and N. Gillett for fieldwork support. We also thank T. Jordan as well as C. Clark and his working group for the discussion on this work. Finally, we thank the scientific editor Olga Sergienko, and three reviewers, Reinhard Drews and two anonymous reviewers, who helped to improve this paper considerably.

References

Ashmore, D. W., Bingham, R. G., Hindmarsh, R. C. A., Corr, H. F. J., & Joughin, I. R. (2014). The relationship between sticky spots and radar reflectivity beneath an active West Antarctic ice stream. *Annals of Glaciology*, *55*(67), 29–38. https://doi.org/10.3189/2014AoG67A052

Atre, S. R., & Bentley, C. R. (1993). Laterally varying basal conditions beneath ice streams B and C, West Antarctica. *Journal of Glaciology*, *39*(133), 507–514. https://doi.org/10.1017/S0022143000016403

Bamber, J. L., Vaughan, D. G., & Joughin, I. (2000). Widespread complex flow in the interior of the Antarctic ice sheet. *Science*, *287*(5456), 1248–1250. https://doi.org/10.1126/science.287.5456.1248

Barcheck, C. G., Schwartz, S. Y., & Tulaczyk, S. (2020). Icequake streaks linked to potential mega-scale glacial lineations beneath an Antarctic ice stream. *Geology*, *48*(2), 99–102. https://doi.org/10.1130/G46626.1

Bentley, C. R., Lord, N., & Liu, C.-J. (1998). Radar reflections reveal a wet bed beneath stagnant Ice Stream C and a frozen bed beneath ridge BC, West Antarctica. *Journal of Glaciology*, *44*(146), 149–156. https://doi.org/10.3189/S0022143000002434

Bindschadler, R., Choi, H., Wichlacz, A., Bingham, R., Bohlander, J., Brunt, K., et al. (2011). Getting around Antarctica: New high-resolution mappings of the grounded and freely-floating boundaries of the Antarctic ice sheet created for the international polar year. *The Cryosphere*, *5*(3), 569–588. https://doi.org/10.5194/tc-5-569-2011

Blankenship, D. D., Morse, D. L., Finn, C. A., Bell, R. E., Peters, M. E., Kempf, S. D., et al. (2001). Geologic controls on the initiation of rapid basal motion for West Antarctic ice streams: A geophysical perspective including new airborne radar sounding and laser altimetry results. In *The West Antarctic Ice Sheet: Behavior and Environment* (Vol. 77, pp. 105–121). https://doi.org/10.1029/AR077p0105

Boulton, A. G. S., Dent, D. L., Morris, E. M., Geografiska, S., Series, A., & Geography, P. (1974). Subglacial shearing and crushing, and the role of water pressures in tills from South-East Iceland. *Geografiska Annaler-Series A: Physical Geography*, *56*(3–4), 135–145. https://doi.org/10.2307/520703

Boulton, G. S. (1976). The origin of glacially fluted surfaces-Observations and theory. *Journal of Glaciology*, *17*(76), 287–309. https://doi.org/10.3189/S0022143000013605

Boulton, G. S., & Dent, D. L. (1974). The nature and rates of post-depositional changes in recently deposited till from south-East Iceland. *Geografiska Annaler-Series A: Physical Geography*, *56*(3–4), 121–134. https://doi.org/10.1080/04353676.1974.11879894

Catania, G. A., Conway, H. B., Gades, A. M., Raymond, C. F., & Engelhardt, H. (2003). Bed reflectivity beneath inactive ice streams in West Antarctica. *Annals of Glaciology*, *36*, 287–291. https://doi.org/10.3189/172756403781816310

Chu, W., Schroeder, D. M., Seroussi, H., Creyts, T. T., Palmer, S. J., & Bell, R. E. (2016). Extensive winter subglacial water storage beneath the Greenland Ice Sheet. *Geophysical Research Letters*, *43*(24), 12484–12492. https://doi.org/10.1002/2016GL071538

Clark, C. D., Tulaczyk, S. M., Stokes, C. R., & Canals, M. (2003). A groove-ploughing theory for the production of mega-scale glacial lineations, and implications for ice-stream mechanics. *Journal of Glaciology*, *49*(165), 240–256. https://doi.org/10.3189/172756503781830719

Clyne, E. R., Anandakrishnan, S., Muto, A., Alley, R. B., & Voigt, D. E. (2020). Interpretation of topography and bed properties beneath Thwaites Glacier, West Antarctica using seismic reflection methods. *Earth and Planetary Science Letters*, *550*(116543). https://doi.org/10.1016/j.epsl.2020.116543

Cooper, M. A., Jordan, T. M., Schroeder, D. M., Siegert, M. J., Williams, C. N., & Bamber, J. L. (2019). Subglacial roughness of the Greenland Ice Sheet: Relationship with contemporary ice velocity and geology. *Cryosphere*, *13*(11), 3093–3115. https://doi.org/10.5194/tc-13-3093-2019

Copland, L., & Sharp, M. (2001). Mapping thermal and hydrological conditions beneath a polythermal glacier with radio-echo sounding. *Journal of Glaciology*, *47*(157), 232–242. https://doi.org/10.3189/172756501781832377

Cuffey, K., & Paterson, W. S. B. (2010). *The Physics of glaciers* (4th ed.). Butterworth-Heinemann. https://doi.org/10.1016/0016-7185(71)90086-8

Daniels, D. J. (1996). Surface-penetrating radar. *Electronics & Communication Engineering Journal*, *8*. https://doi.org/10.1049/ecej:19960402

Davis, J. L., & Annan, A. P. (1989). Ground-Penetrating radar for high-resolution mapping of soil and rock stratigrapphy. *Geophysical Prospecting*, *37*(5), 531–551. https://doi.org/10.1111/j.1365-2478.1989.tb02221.x

Doake, C. S. M., Frolich, R. M., Mantripp, D. R., Smith, a. M., & Vaughan, D. G. (1987). Glaciological studies on Rutford ice stream, Antarctica. *Journal of Geophysical Research*, *92*(B9), 8951. https://doi.org/10.1029/JB092iB09p08951

Dowdeswell, J. A., Canals, M., Jakobsson, M., Todd, B. J., Dowdeswell, E. K., & Hogan, K. A. (2016). The variety and distribution of submarine glacial landforms and implications for ice-sheet reconstruction. *Geological Society, London, Memoirs*, *46*(1), 519–552. https://doi.org/10.1144/M46.183

Ely, J. C., Clark, C. D., Spagnolo, M., Stokes, C. R., Greenwood, S. L., Hughes, A. L. C., et al. (2016). Do subglacial bedforms comprise a size and shape continuum? *Geomorphology*, *257*, 108–119. https://doi.org/10.1016/j.geomorph.2016.01.001

Endres, A. L., Murray, T., Booth, A. D., & West, L. J. (2009). A new framework for estimating englacial water content and pore geometry using combined radar and seismic wave velocities. *Geophysical Research Letters*, *36*(4), 1–5. https://doi.org/10.1029/2008GL036876

Evans, D. J. A., Phillips, E. R., Hiemstra, J. F., & Auton, C. A. (2006). Subglacial till: Formation, sedimentary characteristics and classification. *Earth-Science Reviews*, *78*(1–2), 115–176. https://doi.org/10.1016/j.earscirev.2006.04.001

Everest, J., Bradwell, T., & Golledge, N. (2005). Subglacial landforms of the tweed palaeo-ice stream. *Scottish Geographical Journal*, *121*(2), 163–173. https://doi.org/10.1080/00369220518737229

Foley, N., Tulaczyk, S., Auken, E., Schamper, C., Dugan, H., Mikucki, J., et al. (2016). Helicopter-borne transient electromagnetics in high-latitude environments: An application in the McMurdo Dry Valleys, Antarctica. *Geophysics*, *81*(1), WA87. https://doi.org/10.1190/geo2015-0186.1

Fujita, S., Maeno, H., & Matsuoka, K. (2006). Radio-wave depolarization and scattering within ice sheets: A matrix-based model to link radar and ice-core measurements and its application. *Journal of Glaciology*, *52*(178), 407–424. https://doi.org/10.3189/172756506781828548

Gades, A. M., Raymond, C. F., Conway, H., & Jagobel, R. W. (2000). Bed properties of Siple Dome and adjacent ice streams, West Antarctica, inferred from radio-echo sounding measurements. *Journal of Glaciology*, *46*(152), 88–94. https://doi.org/10.3189/172756500781833467

Gardner, G. H. F., Gardner, L. W., & Gregory, A. R. (1974). Formation velocity and density—the diagnostic basics for stratigraphic traps. *Geophysics*, *39*(6), 770–780. https://doi.org/10.1190/1.1440465

Ghose, R., & Slob, E. C. (2006). Quantitative integration of seismic and GPR reflections to derive unique estimates for water saturation and porosity in subsoil. *Geophysical Research Letters*, *33*(5), L05404. https://doi.org/10.1029/2005GL025376

Grima, C., Kofman, W., Herique, A., Orosei, R., & Seu, R. (2012). Quantitative analysis of Mars surface radar reflectivity at 20MHz. *Icarus*, *220*(1), 84–99. https://doi.org/10.1016/j.icarus.2012.04.017

Gudmundsson, G. H. (2006). Fortnightly variations in the flow velocity of Rutford ice stream, West Antarctica. *Nature*, *444*(7122), 1063–1064. https://doi.org/10.1038/nature05430

Gudmundsson, G. H., & Jenkins, A. (2009). Ice-flow velocities on Rutford ice stream, West Antarctica, are stable over decadal timescales. *Journal of Glaciology*, *55*(190), 339–344. https://doi.org/10.3189/002214309788608697

Holland, C. W., & Anandakrishnan, S. (2009). Subglacial seismic reflection strategies when source amplitude and medium attenuation are poorly known. *Journal of Glaciology*, *55*(193), 931–937. https://doi.org/10.3189/002214309790152528

Holschuh, N., Christianson, K., Paden, J., Alley, R. B., & Anandakrishnan, S. (2020). Linking postglacial landscapes to glacier dynamics using swath radar at Thwaites Glacier, Antarctica. *Geology*, *48*(3), 268–272. https://doi.org/10.1130/G46772.1

Jacobel, R. W., Lapo, K. E., Stamp, J. R., Youngblood, B. W., Welch, B. C., & Bamber, J. L. (2010). A comparison of basal reflectivity and ice velocity in East Antarctica. *The Cryosphere*, *4*(4), 447–452. https://doi.org/10.5194/tc-4-447-2010

Jacobel, R. W., Welch, B. C., Osterhouse, D., Pettersson, R., & MacGregor, J. A. (2009). Spatial variation of radar-derived basal conditions on Kamb ice stream, West Antarctica. *Annals of Glaciology*, *50*(51), 10–16. https://doi.org/10.3189/172756409789097504

Joughin, I., Bamber, J. L., Scambos, T., Tulaczyk, S., Fahnestock, M., & MacAyeal, D. R. (2006). Integrating satellite observations with modelling: Basal shear stress of the Filcher-Ronne ice streams, Antarctica. *Philosophical Transactions of the Royal Society A: Mathematical, Physical & Engineering Sciences*, *364*(1844), 1795–1814. https://doi.org/10.1098/rsta.2006.1799

Kamb, B. (2001). Basal zone of the West Antarctic ice streams and its role in lubrication of their rapid motion. *The West Antarctic Ice Sheet: Behavior and Environment; Antarctic Research Series*, *7*(77), 157–199. https://doi.org/10.1029/AR077p0157

King, E. C., Hindmarsh, R. C. A., & Stokes, C. R. (2009). Formation of mega-scale glacial lineations observed beneath a West Antarctic ice stream. *Nature Geoscience*, *2*(8), 585–588. https://doi.org/10.1038/ngeo581

King, E. C., Pritchard, H. D., & Smith, A. M. (2016). Subglacial landforms beneath Rutford ice stream, Antarctica: Detailed bed topography from ice-penetrating radar. *Earth System Science Data*, *8*(1), 151–158. https://doi.org/10.5194/essd-8-151-2016

King, E. C., Woodward, J., & Smith, A. M. (2007). Seismic and radar observations of subglacial bed forms beneath the onset zone of Rutford Ice Stream, Antarctica. *Journal of Glaciology*, *53*(183), 665–672. https://doi.org/10.3189/002214307784409216

Knoll, M. D. (1996). *A petrophysical basis for ground penetrating radar and very early time electromagnetics: Electrical properties of sand-clay mixtures*. University of British Columbia. https://doi.org/10.14288/1.0052324

Kufner, S.-K., Brisbourne, A. M., Smith, A. M., Hudson, T. S., Murray, T., Schlegel, R., et al. (2021). Not all icequakes are created equal: Basal icequakes suggest diverse bed deformation mechanisms at Rutford ice stream, West Antarctica. *Journal of Geophysical Research: Earth Surface*, *126*. https://doi.org/10.1029/2020JF006001

MacGregor, J. A., Catania, G. A., Conway, H., Schroeder, D. M., Joughin, I., Young, D. A., et al. (2013). Weak bed control of the eastern shear margin of Thwaites Glacier, West Antarctica. *Journal of Glaciology*, *59*(217), 900–912. https://doi.org/10.3189/2013JoG13J050

Martinez, A., & Byrnes, A. P. (2001). Modeling dielectric-constant values of geologic materials: An aid to ground-penetrating radar data collection and interpretation. *Current Research in Earth Sciences*, *247*(1), 1–16. https://doi.org/10.17161/cres.v0i247.11831

Matsuoka, K. (2011). Pitfalls in radar diagnosis of ice-sheet bed conditions: Lessons from englacial attenuation models. *Geophysical Research Letters*, *38*(5), L05505. https://doi.org/10.1029/2010GL046205

McCabe, A. M., & Dardis, G. F. (1994). Glaciotectonically induced water-throughflow structures in a late pleistocene drumlin, Kanrawer, county galway, western Ireland. *Sedimentary Geology*, *91*(1–4), 173–190. https://doi.org/10.1016/0037-0738(94)90128-7

Mount, G. J., & Comas, X. (2014). Estimating porosity and solid dielectric permittivity in the Miami Limestone using high-frequency ground penetrating radar (GPR) measurements at the laboratory scale. *Water Resources Research*, *50*(10), 7590–7605. https://doi.org/10.1002/2013WR014947

Murray, T., Corr, H., Forieri, A., & Smith, A. M. (2008). Contrasts in hydrology between regions of basal deformation and sliding beneath Rutford Ice Stream, West Antarctica, mapped using radar and seismic data. *Geophysical Research Letters*, *35*(12), 1–5. https://doi.org/10.1029/2008GL033681

Murray, T., Smith, A. M., King, M. A., & Weedon, G. P. (2007). Ice flow modulated by tides at up to annual periods at Rutford Ice Stream, West Antarctica. *Geophysical Research Letters*, *34*(18), 1–6. https://doi.org/10.1029/2007GL031207

Muto, A., Anandakrishnan, S., Alley, R. B., Horgan, H. J., Parizek, B. R., Koellner, S., et al. (2019). Relating bed character and subglacial morphology using seismic data from Thwaites Glacier, West Antarctica. *Earth and Planetary Science Letters*, *507*, 199–206. https://doi.org/10.1016/j.epsl.2018.12.008

Navarro, F. J., Macheret, Y. Y., & Benjumea, B. (2005). Application of radar and seismic methods for the investigation of temperate glaciers. *Journal of Applied Geophysics*, *57*(3), 193–211. https://doi.org/10.1016/j.jappgeo.2004.11.002

Piotrowski, J. A., & Kraus, A. M. (1997). Response of sediment to ice-sheet loading in northwestern Germany: Effective stresses and glacier-bed stability. *Journal of Glaciology*, *43*(145), 495–502. https://doi.org/10.1017/S0022143000035103

Piotrowski, J. A., Larsen, N. K., & Junge, F. W. (2004). Reflections on soft subglacial beds as a mosaic of deforming and stable spots. *Quaternary Science Reviews*, *23*(9–10), 993–1000. https://doi.org/10.1016/j.quascirev.2004.01.006

Reynolds, J. M. (1997). *An introduction to applied and environmental geophysics*. John Wiley and Sons.

Rignot, E. (2008). Changes in West Antarctic ice stream dynamics observed with ALOS PALSAR data. *Geophysical Research Letters*, *35*(12), L12505. https://doi.org/10.1029/2008GL033365

Riverman, K. L., Anandakrishnan, S., Alley, R. B., Holschuh, N., Dow, C. F., Muto, A., et al. (2019). Wet subglacial bedforms of the NE Greenland Ice Stream shear margins. *Annals of Glaciology*, *60*(80), 91–99. https://doi.org/10.1017/aog.2019.43

Roth, K., Schulin, R., Flühler, H., & Attinger, W. (1990). Calibration of time domain reflectometry for water content measurement using a composite dielectric approach. *Water Resources Research*, *26*(10), 2267–2273. https://doi.org/10.1029/WR026i010p02267

Salisbury, M. H., Harvey, C. W., & Matthews, L. (2003). The acoustic properties of Ores and Host rocks in Hardrock Terranes. In *Hardrock seismic exploration* (pp. 9–19). Society of Exploration Geophysicists. https://doi.org/10.1190/1.9781560802396.ch1

Schlegel, R., Brisbourne, A., King, E., Murray, T., & Smith, A. (2020). Radar-derived bed reflectivity of Rutford ice stream, West Antarctica, December 2016 to January 2017 (Version 1.0) [Dataset]. UK Polar Data Centre, Natural Environment Research Council. https://doi.org/10.5285/5F68FCE1-863E-4173-ACDB-0ED03CCA1C95

Schoof, C. G., & Clarke, G. K. C. (2008). A model for spiral flows in basal ice and the formation of subglacial flutes based on a Reiner-Rivlin rheology for glacial ice. *Journal of Geophysical Research: Solid Earth*, *113*(5), 1–12. https://doi.org/10.1029/2007JB004957

Schroeder, D. M., Blankenship, D. D., & Young, D. A. (2013). Evidence for a water system transition beneath Thwaites glacier, West Antarctica. *Proceedings of the National Academy of Sciences*, *110*(30), 12225–12228. https://doi.org/10.1073/pnas.1302828110

Schroeder, D. M., Seroussi, H., Chu, W., & Young, D. A. (2016). Adaptively constraining radar attenuation and temperature across the Thwaites Glacier catchment using bed echoes. *Journal of Glaciology*, *62*(236), 1075–1082. https://doi.org/10.1017/jog.2016.100

Shaw, J., Pugin, A., & Young, R. R. (2008). A meltwater origin for Antarctic shelf bedforms with special attention to megalineations. *Geomorphology*, *102*(3–4), 364–375. https://doi.org/10.1016/j.geomorph.2008.04.005

Siegert, M. J., Kulessa, B., Bougamont, M., Christoffersen, P., Key, K., Andersen, K. R., et al. (2018). Antarctic subglacial groundwater: A concept paper on its measurement and potential influence on ice flow. *Geological Society, London, Special Publications*, *461*(1), 197–213. https://doi.org/10.1144/SP461.8

Siegert, M. J., & Ridley, J. K. (1998). Determining basal ice-sheet conditions in the Dome C region of East Antarctica using satellite radar altimetry and airborne radio-echo sounding. *Journal of Glaciology*, *44*(146), 1–8. https://doi.org/10.3189/S002214300000229X

Smith, A. M. (1997a). Basal conditions on Rufford ice stream, West Antarctica, from seismic observations. *Journal of Geophysical Research*, *102*(B1), 543–552. https://doi.org/10.1029/96jb02933

Smith, A. M. (1997b). Variations in basal conditions on Rutford ice stream, west Antarctica. *Journal of Glaciology*, *43*(144), 245–255. https://doi.org/10.1017/s0022143000003191

Smith, A. M., Anker, P. G. D., Nicholls, K. W., Makinson, K., Murray, T., Rios-Costas, S., et al. (2020). Ice stream subglacial access for ice-sheet history and fast ice flow: The BEAMISH project on Rutford ice stream, West Antarctica and initial results on basal conditions. *Annals of Glaciology*, *61*(83), 1–9. https://doi.org/10.1017/aog.2020.82

Smith, A. M., & Murray, T. (2009). Bedform topography and basal conditions beneath a fast-flowing West Antarctic ice stream. *Quaternary Science Reviews*, *28*(7–8), 584–596. https://doi.org/10.1016/j.quascirev.2008.05.010

Smith, A. M., Murray, T., Nicholls, K. W., Makinson, K., Adalgeirsdóttir, G., Behar, A. E., & Vaughan, D. G. (2007). Rapid erosion, drumlin formation, and changing hydrology beneath an Antarctic ice stream. *Geology*, *35*(2), 127–130. https://doi.org/10.1130/G23036A.1

Smith, A. M., Woodward, J., Ross, N., Bentley, M. J., Hodgson, D. A., Siegert, M. J., & King, E. C. (2018). Evidence for the long-term sedimentary environment in an Antarctic subglacial lake. *Earth and Planetary Science Letters*, *504*, 139–151. https://doi.org/10.1016/j.epsl.2018.10.011

Smith, E. C., Smith, A. M., White, R. S., Brisbourne, A. M., & Pritchard, H. D. (2015). Mapping the ice-bed interface characteristics of Rutford Ice Stream, West Antarctica, using microseismicity. *Journal of Geophysical Research: Earth Surface*, *120*(9), 1881–1894. https://doi.org/10.1002/2015JF003587

Spagnolo, M., Clark, C. D., Ely, J. C., Stokes, C. R., Anderson, J. B., Andreassen, K., et al. (2014). Size, shape and spatial arrangement of mega-scale glacial lineations from a large and diverse dataset. *Earth Surface Processes and Landforms*, *39*(11), 1432–1448. https://doi.org/10.1002/esp.3532

Tulaczyk, S., & Foley, N. (2020). The role of electrical conductivity in radarwave reflection. *The Cryosphere Discussions*, *14*(12). https://doi.org/10.5194/tc-2020-9

Ulaby, F. T., Moore, R. K., & Fung, A. K. (1982). *Microwave remote sensing: Active and passive, volume II. Radar remote sensing and surface scattering and emission theory. Volume II. Radar remote sensing and surface scattering and emission theory*.

Vaughan, D. G., Corr, H. F. J., Smith, A. M., Pritchard, H. D., & Shepherd, A. (2008). Flow-switching and water piracy between Rutford Ice stream and Carlson inlet, West Antarctica. *Journal of Glaciology*, *54*(184), 41–48. https://doi.org/10.3189/002214308784409125

West, L. J., Handley, K., Huang, Y., & Pokar, M. (2003). Radar frequency dielectric dispersion in sandstone: Implications for determination of moisture and clay content. *Water Resources Research*, *39*(2), 1–12. https://doi.org/10.1029/2001WR000923

Winebrenner, D. P., Smith, B. E., Catania, G. A., Conway, H. B., & Raymond, C. F. (2003). Radio-frequency attenuation beneath Siple Dome, West Antarctica, from wide-angle and profiling radar observations. *Annals of Glaciology*, *37*, 226–232. https://doi.org/10.3189/172756403781815483

Reference From the Supporting Information

York, D., Evensen, N. M., Martinez, M. L., & De Basabe Delgado, J. (2004). Unified equations for the slope, intercept, and standard errors of the best straight line. *American Journal of Physics*, *72*(3), 367–375. https://doi.org/10.1119/1.1632486